ENGINEERING

Stretchable elastic synaptic transistors for neurologically integrated soft engineering systems

Hyunseok Shim[1], Kyoseung Sim[1], Faheem Ershad[2], Pinyi Yang[3], Anish Thukral[3], Zhoulyu Rao[1], Hae-Jin Kim[3,4], Yanghui Liu[5], Xu Wang[1], Guoying Gu[6], Li Gao[7], Xinran Wang[8], Yang Chai[5], Cunjiang Yu[1,2,3,9]*

Artificial synaptic devices that can be stretched similar to those appearing in soft-bodied animals, such as earthworms, could be seamlessly integrated onto soft machines toward enabled neurological functions. Here, we report a stretchable synaptic transistor fully based on elastomeric electronic materials, which exhibits a full set of synaptic characteristics. These characteristics retained even the rubbery synapse that is stretched by 50%. By implementing stretchable synaptic transistor with mechanoreceptor in an array format, we developed a deformable sensory skin, where the mechanoreceptors interface the external stimulations and generate presynaptic pulses and then the synaptic transistors render postsynaptic potentials. Furthermore, we demonstrated a soft adaptive neurorobot that is able to perform adaptive locomotion based on robotic memory in a programmable manner upon physically tapping the skin. Our rubbery synaptic transistor and neurologically integrated devices pave the way toward enabled neurological functions in soft machines and other applications.

INTRODUCTION

Notable progresses have been made in developing soft machines, robotics, or engineering systems to mimic soft animals (*1–3*). Neurologic functions, however, have never been realized in these artificial systems. Synapses are unique and critical biological structures that allow for the transmission of electrical or chemical signals thus to enable neurons to communicate with each other and are responsible for encoding sensations, thoughts, etc. (*4, 5*). Embodied within humans or animals, the synapse is usually soft and able to accommodate various forms of mechanical deformations (*6*). In particular, some soft-bodied animals have very stretchy synapses that can elongate to a significant extent (*7, 8*). For instance, earthworms have very stretchable (by 50 to 100%) nerves that elicit different responses based on the interactions with the surrounding environment (*9*), as illustrated in Fig. 1A. The understandings in biology and advances in materials and electronic technologies have led to the recent development of artificial synaptic devices, mostly in rigid or flexible formats (*10–17*), to emulate the biological counterparts toward emerging applications, such as parallel processing (*18–23*), low-power computing (*10, 24*), neuroprosthetics (*11, 25*), etc. Artificial synapses, which are very stretchable similar to those that

appear in soft animals, are key to enabled neurological functions in soft machines and many other applications, such as neuroprosthetics (*11, 26–29*). Only a handful of studies have reported stretchable synaptic devices (*30, 31*). However, a stretchable synaptic device, in particular, one that is all based on intrinsically stretchable soft materials, has never been reported before.

Here, we report a stretchable synaptic transistor and its neurologically integrated devices made fully from rubbery materials. Specifically, we developed the fully rubbery synaptic transistor using rubbery semiconductor from composite of poly(3-hexylthiophene) (P3HT) nanofibrils percolated in polydimethylsiloxane (P3HT-NFs/PDMS), rubbery conductor from percolated composite of Au nanoparticle–decorated silver nanowires in PDMS (AuNPs-AgNWs/PDMS), and elastic gate dielectric from ion gel. The synaptic transistor exhibits similar functions as those of biological synapses, including excitatory postsynaptic current (EPSC), paired-pulse facilitation (PPF), short-term memory (STM), long-term memory (LTM), and filter characteristics. Upon mechanical stretching by 50%, these characteristics still remained. In addition, we developed a neurologically integrated tactile sensory skin in fully rubbery format based on an array of mechanoreceptors of pressure-sensitive rubber and fully rubbery synaptic transistors. The mechanoreceptors respond to physical touches by generating presynaptic pulses, which excite the synaptic transistors to render postsynaptic potentials, which can be potentially interfaced with biological nerves or engineering counterparts. Postsynaptic potential mapping from the arrayed sensory pixels was achieved even when the skin is stretched. We further created a soft adaptive neurologically integrated robot, i.e., neurorobot, which is constructed on the basis of a soft pneumatic robot covered with functional elastic skins of the triboelectric nanogenerators (TENGs) and synaptic transistors. The robot senses physical tapping and locomotes adaptively in a programmed manner through synapse memory encoded signals. Systematic studies of the device construction and operation mechanism components and neurologically integrated systems reveal all the fundamental aspects and also suggest their future usages.

[1]Materials Science and Engineering Program, University of Houston, Houston, TX 77204, USA. [2]Department of Biomedical Engineering, University of Houston, Houston, TX 77204, USA. [3]Department of Mechanical Engineering, University of Houston, Houston, TX 77204, USA. [4]School of Mechanical and Aerospace Engineering, Gyeongsang National University, 501, Jinju-daero, Jinju, Gyeongnam 52828, Korea. [5]Department of Applied Physics, The Hong Kong Polytechnic University, Kowloon, Hong Kong, China. [6]State Key Laboratory of Mechanical System and Vibration, Robotics Institute, and School of Mechanical Engineering, Shanghai Jiao Tong University, Shanghai 200240, China. [7]Key Laboratory for Organic Electronics and Information Displays (KLOEID), Institute of Advanced Materials (IAM), and School of Materials Science and Engineering, Nanjing University of Posts and Telecommunications, 9 Wenyuan Road, Nanjing 210046, China. [8]National Laboratory of Solid State Microstructures, School of Electronic Science and Engineering, Collaborative Innovation Center of Advanced Microstructures, Nanjing University, Nanjing 210093, China. [9]Department of Electrical and Computer Engineering, Texas Center for Superconductivity, University of Houston, Houston, TX 77204, USA.
*Corresponding author. Email: cyu15@uh.edu
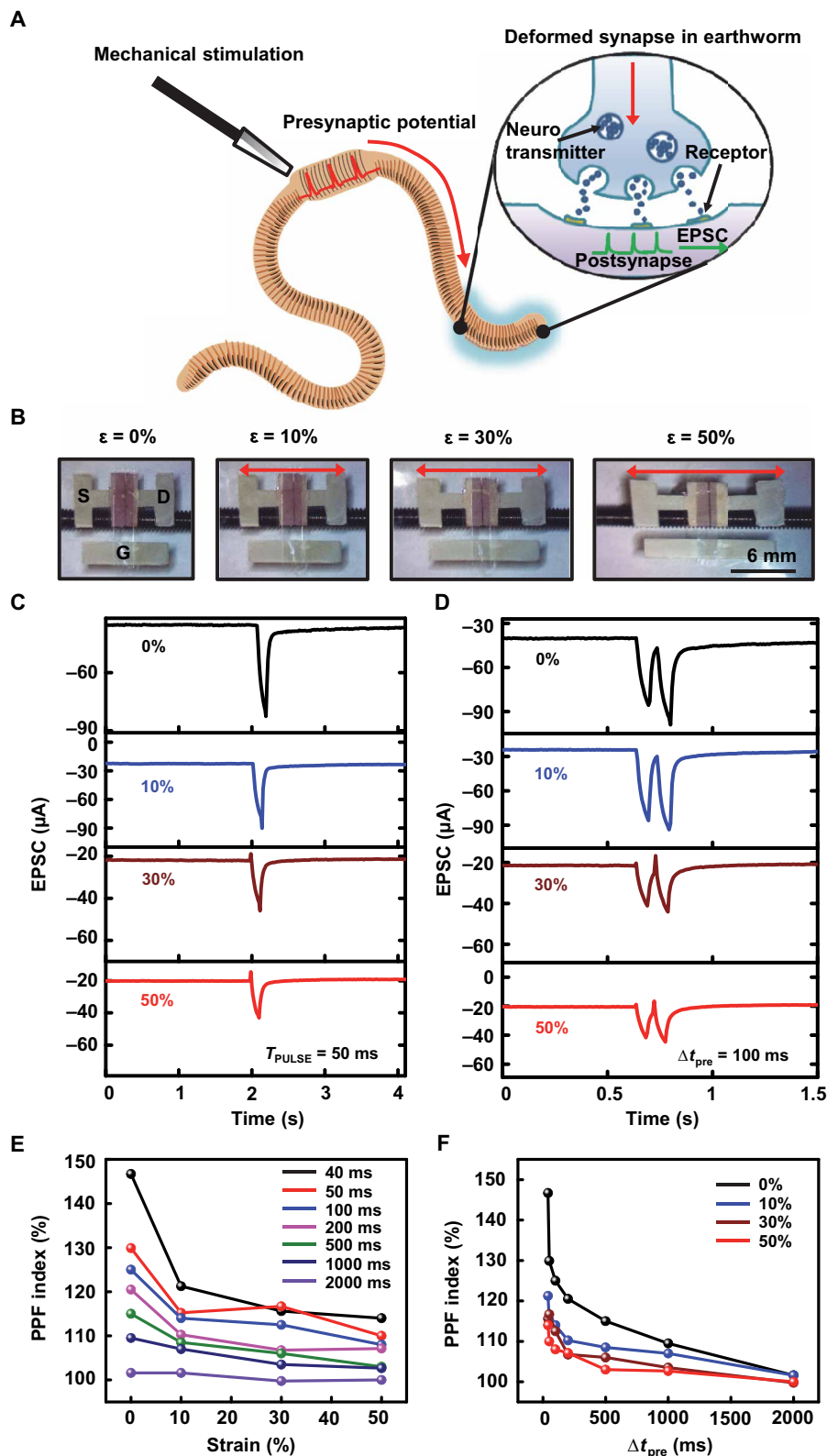
Fig. 1. Fully rubbery synaptic transistors. (**A**) Schematic illustration of the deformable synapse and its synaptic transmission process in an earthworm. (**B**) Optical images of the fully rubbery synaptic transistor under different levels (0, 10, 30, and 50%) of mechanical strain. (**C**) Single presynaptic pulse induced EPSC under different levels of mechanical strain. (**D**) The EPSC triggered by two successive presynaptic pulses under different levels of mechanical strain. (**E**) PPF results with respect to the applied strain for pulse with various pulse interval Δt_{pre}. (**F**) PPF results with respect to the different Δt_{pre} under different levels of applied strain (Photo Credit: Hyunseok Shim, University of Houston).

RESULTS

Rubbery synaptic transistor

Figure 1A shows a schematic illustration of stretchy and deformable synapse and its synaptic transmission process in an earthworm. The nerve impulses from mechanical stimulations are generated in the presynaptic neuron, and then, ion channels of the postsynapse start to open. The vesicles containing the neurotransmitters move toward the end of the axon, and the neurotransmitters are freed to move through the synaptic cleft (32). The neurotransmitters unite with the receptors on the postsynaptic neuron, which allows the ions to move across the membrane of the postsynaptic neuron and generate postsynaptic potential. In our synaptic transistor, the ions from the ion gel and the channel conductance mimic the biological neuro transmitters and the synaptic weight, respectively.

We constructed the rubbery synaptic transistors using P3HT-NFs/PDMS, ion gel, and rubbery conductor AuNPs-AgNWs/PDMS. All of them are stretchy similar to a rubber band (fig. S1). The detailed material preparation is presented in Materials and Methods. We fabricated the devices based on solution processes in a layer-by-layer manner. The specific capacitance per unit area of the ion gel is measured to be ~7 μF/cm^2 at low-frequency region and ~1 μF/cm^2 at 10 kHz (fig. S2). Specifically, the synaptic transistor is constructed into a top-gated device on the PDMS substrate, with partially embedded AuNPs-AgNWs electrodes. It is noted that the galvanic replacement process enables the coating of AuNPs on the AgNWs so that the work function of the electrode is comparable to the highest occupied molecular orbital (HOMO) level of the P3HT-NFs/PDMS semiconductor to form ohmic contact (33). The schematic architecture and operational diagram of the synaptic transistor are shown in fig. S3. When a presynaptic pulse is applied to the gate, a postsynaptic current will be induced.

Figure 1B shows a set of optical images of the fully rubbery synaptic transistor before and after uniaxial stretching by 10, 30, and 50% along the channel length direction. The thickness of the P3HT-NFs/PDMS layer is ~280 nm. The channel length and the width are 60 μm and 3 mm, respectively. The transfer curves of the device under different levels of strain are shown in fig. S4A. The calculated mobility and threshold voltage with respect to mechanical strain are shown in fig. S4B. The detailed calculations are presented in the Supplementary Materials.

To characterize the single pulse–induced EPSC, we apply a presynaptic pulse (−3 V, 50 ms) on the gate with a V_{ds} of −1 V. The ions are accumulated at the interface of ion gel upon applying presynaptic pulse. At the end of the first pulse, the channel conductance gradually reaches equilibrium due to the relaxation (34, 35). The EPSC results of the fully rubbery synaptic transistor are plotted in Fig. 1C. The EPSC of the unstretched synaptic transistor is 82.21 μA. Upon stretching by 10, 30, and 50%, the EPSC decreased to 77.15, 44.54, and 41.8 μA, respectively. When the device is stretched by 50%, the EPSC retained by about 50%. The decrease in EPSC when the device is stretched is similar to that of the ON current, which is mainly attributed to the channel geometry change and the ruptures of P3HT-NF (36). The detailed EPSC results with different pulse widths are listed in fig. S5.

We further tested the EPSC under two successive presynaptic pulses with pulse interval (Δt_{pre}) ranging from 40 to 2000 ms. Figure 1D exhibits the EPSC results triggered by two successive presynaptic pulses with Δt_{pre} of 100 ms. The EPSC peak from the second pulse is greater than that from the first presynaptic pulse. The PPF index is defined as the ratio between the amplitude of the second EPSC (A_2) and the first EPSC (A_1). When the device is stretched by 50%, the PPF index retained by 107%. The detailed EPSC results with fixed duty cycle of 50%, yet different Δt_{pre} are listed in fig. S6. The PPF index depending on strains with various pulse widths is shown in Fig. 1E. A maximum PPF index of ~146% was obtained with Δt_{pre} = 40 ms under 0% strain. As Δt_{pre} decreases, part of the induced ions in the first pulse still exists at the interface between ion gel and channel, which resulted in higher conductance and, thus, high EPSC for the second pulse. Therefore, we achieved a higher PPF index. When the strain increased, the PPF index decreased gradually to 114% at the strain of 50%. The PPF index with different Δt_{pre} under different levels of strain is plotted in Fig. 1F. The PPF index decreased as Δt_{pre} increased from 40 to 2000 ms and remained ~100% for the Δt_{pre} of 2000 ms for synaptic transistor stretched by 50%. The lower PPF from long Δt_{pre} is due to the relaxation of the ions. It is noted that a similar trend of degradation of EPSCs was observed, as shown in fig. S7, when the rubbery synaptic transistor was stretched along the channel width direction.

Biological synapses have filtering characteristics, important feats for neurons to transmit signals (37). Figure 2A schematically illustrates the filtering behavior of the synaptic transistor. When multiple successive presynaptic pulses are applied to the synaptic transistor, a synaptic weight change (current) can be generated. By changing the frequency of the presynaptic pulses, different EPSC amplitudes would be obtained (38, 39). If the EPSC amplitude is higher than the threshold, then the synapse will fire an action potential (40), which indicates high-pass filtering behavior (Fig. 2B).

We systematically studied the synaptic filtering characteristics. Specifically, we chose pulses with different frequencies ranging from 1 to 20 Hz to illustrate the high-pass filtering characteristics. We kept the drain voltage at −1 V for all pulses during the measurement. We tested the rubbery synaptic transistor without and with (50%) strain. Figure 2C shows the representative EPSC results for applying 20 successive presynaptic pulses with a width of 35 ms, a frequency of 20 Hz, and an amplitude of −3 V. The EPSCs for the device nonstretched and stretched by 50% are marked in black and red, respectively. The gain of EPSC is defined as A_{20}/A_1, as indicated in Fig. 2D. Figure 2E summarizes the calculated gain with respect to different frequencies. For the rubbery synaptic transistor, without stretch, the gain increased from 1.03 to 2.3 when the frequency increased from 1 to 20 Hz. The detailed EPSC results are shown in fig. S8. Upon stretching by 50%, high-pass filtering characteristics still existed. The gain increased from 1.01 to 1.82 as the frequency increases from 1 to 20 Hz. It is noted that gain experienced some decrease upon stretching by 50%. This is mainly because the output current decreases as of the applied strain, observed elsewhere (36). Figure 2F presents the peak current of the EPSCs with respect to each pulse for the synaptic transistor with (50%) and without strain. The peak current increased as the pulse number increased. However, upon stretching by 50%, the peak current is lower than that of the unstretched device, attributing to the same reason aforementioned.

Besides the synaptic (i.e., EPSCs and filter characteristics) behaviors as mentioned above, other key features of the synaptic transistor such as sensory memory (SM), STM, and LTM, existing in nerves (12, 41–43), were also characterized. As schematically shown in Fig. 3A, the EPSC, i.e., memory strength, gradually increases during the successive presynaptic pulse input. The first and the last EPSC peaks are denoted as w_1 and w_n, respectively. The initial current (before presynaptic pulse) and current change (after presynaptic pulse) are
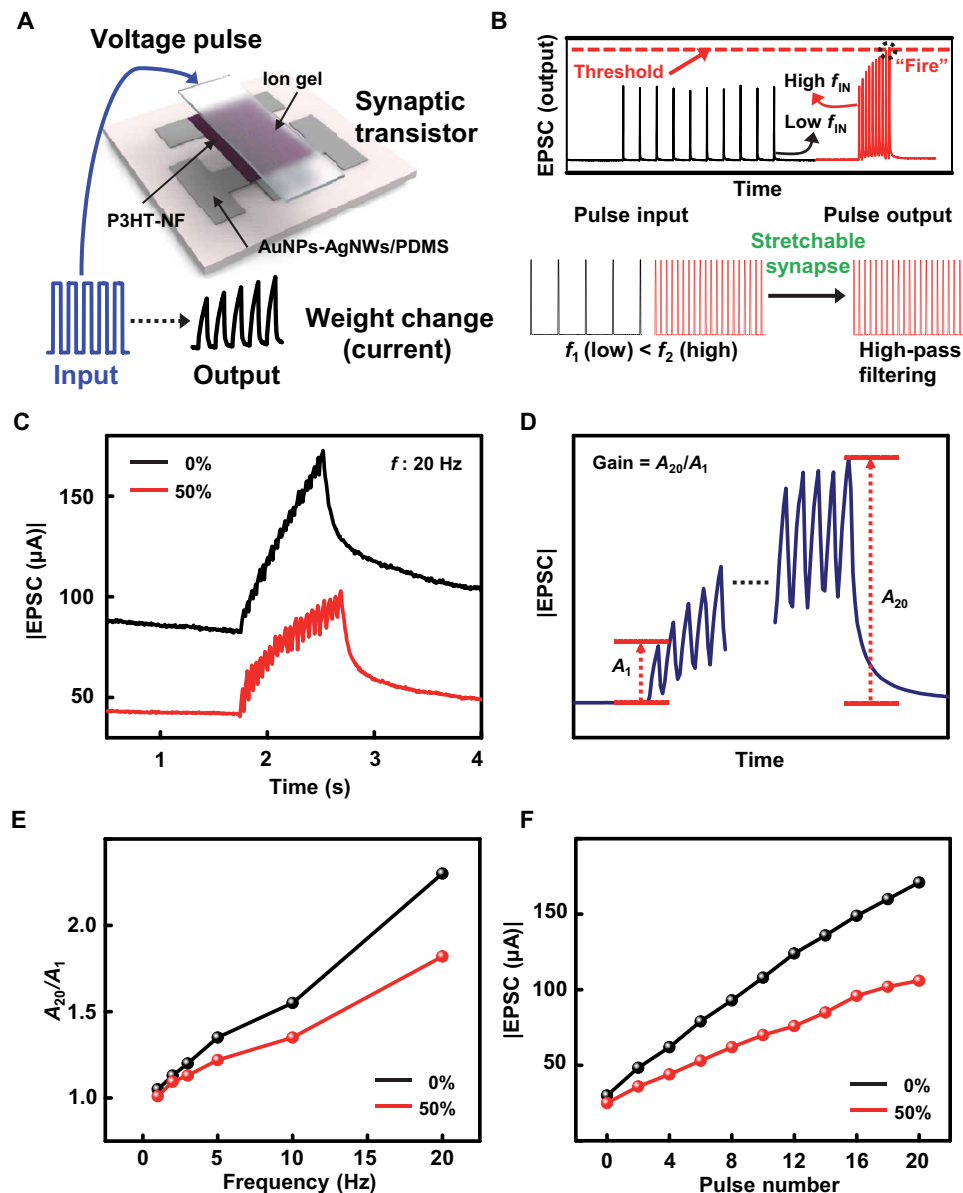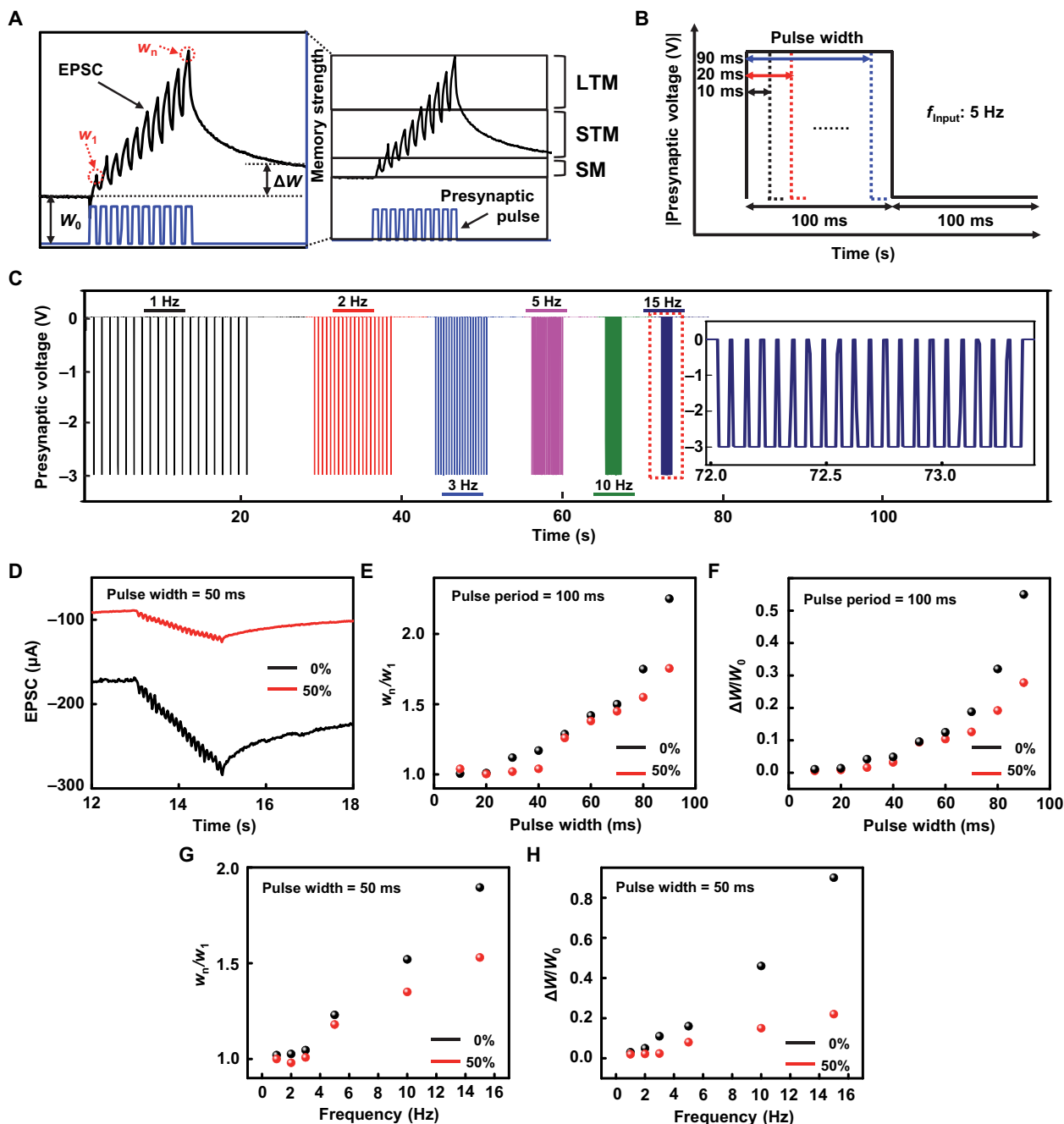
Fig. 2. The filtering characteristics of the fully rubbery synaptic transistor. (**A**) Schematic device structure and demonstration of multiple presynaptic pulses induced synaptic transistor responses. (**B**) Illustration of high-pass filtering behavior. (**C**) Measured EPSCs in response to 20 successive presynaptic pulses at 20 Hz without (0%) and with strains of 50%. (**D**) Illustration of EPSC induced by multiple presynaptic pulses and the definition of the gain (A_{20}/A_1). (**E**) The gain of the EPSCs (A_{20}/A_1) with respect to different pulse frequencies of the fully rubbery synaptic transistor without (0%) and with strains of 50%. (**F**) The peak current of the EPSC with respect to the number of pulses for the rubbery synaptic transistor without (0%) and with strains of 50%.

denoted as W_0 and ΔW, respectively. The short-term weight change is defined as w_n/w_1. The long-term weight change, i.e., the relative synaptic weight change, is calculated on the basis of $\Delta W/W_0$.

Figure 3 (B and C) shows two sets of 20 successive presynaptic pulses used to investigate the STM and LTM characteristics of the fully rubbery synaptic transistors. The first set included nine different input pulses with a fixed frequency of 5 Hz yet increased widths from 10 to 90 ms with the step of 10 ms (Fig. 3B). The second set had fixed pulse width of 50 ms yet with variable frequencies from 1 to 15 Hz (Fig. 3C). Figure 3D shows the EPSC results of the fully rubbery synaptic transistor without (0%; black) and with 50% strain (red) with the application of the 20 successive presynaptic pulses with a

pulse width of 50 ms, a pulse frequency of 10 Hz, and an amplitude of −3 V. The results indicate that both STM and LTM characteristics exist. With 50% applied strain, the overall EPSC decreased, the w_n/w_1 decreased from 1.55 (0% strain) to 1.34 (50% strain), and the $\Delta W/W_0$ decreased from 0.46 (0% strain) to 0.15 (50% strain).

Figure 3E shows the short-term weight change w_n/w_1 results of the fully rubbery synaptic transistor with 0 and 50% strain upon the application of the first set of pulses. As the pulse width increases, w_n/w_1 also increases. Presynaptic pulses with longer pulse widths result in more ions migrated to the ion gel/P3HT-NF channel interface. The detailed EPSC results for different pulse widths are shown in fig. S9. As the pulse width increases, $\Delta W/W_0$ also increases, as shown in Fig. 3F.

Fig. 3. The memory characteristics of the fully rubbery synaptic transistor. (**A**) Scheme of the SM, STM, and LTM. (**B** and **C**) Presynaptic pulses with variable pulse width and frequencies. (**D**) Memory characteristic of the full rubbery synaptic transistor under mechanical strains of 0 and 50% with the application of the 20 successive presynaptic pulses with a pulse width of 50 ms, a pulse frequency of 10 Hz, and an amplitude of −3 V. (**E**) The short-term weight change w_n/w_1 of the fully rubbery synaptic transistor corresponding to different pulse widths without (0%) and with 50% strain. (**F**) The long-term weight change $\Delta W/W_0$ of the fully rubbery synaptic transistor with respect to different pulse widths without (0%) and with 50% strain. (**G**) The w_n/w_1 of the fully rubbery synaptic transistor with respect to different pulse frequencies yet a fixed pulse width of 50 ms without (0%) and with 50% strain. (**H**) The $\Delta W/W_0$ of the fully rubbery synaptic transistor with respect to different pulse frequencies yet a fixed pulse width of 50 ms without (0%) and with 50% strain.

Upon the application of the second set of pulses with increased frequency, the EPSC increases for conditions with (50%) and without strain, as shown in fig. S10. Both the w_n/w_1 and $\Delta W/W_0$ increased as the pulse frequency increased, as shown in Fig. 3 (G and H, respectively). The governing mechanism is the same as that of PPF index as mentioned before. It is noted that the w_n/w_1 and $\Delta W/W_0$ of the synaptic transistor upon applied 50% strain are lower than those of

the device without applied strain. These results suggest that the rubbery stretchable synaptic transistor still retains STM and LTM characteristics even at 50% strain.

Deformable neurologically integrated tactile sensory skin
We developed a stretchable artificial synapse–implemented tactile sensory skin in fully rubbery format to illustrate its potential usages.

This sensory skin is based on the all rubbery mechanoreceptor and synaptic transistors. The action potentials created by the sensory receptor is transmitted in the form of pulses to the artificial synapse to be potentially interfaced with biological nerves and engineering counterparts, as illustrated in Fig. 4A.

Specifically, a 5 by 5 arrayed rubbery sensory array skin was constructed with a four-layer structure: a patterned gate electrode (first), pressure-sensitive rubber (second) connected to the gate electrodes of the rubbery synaptic transistor array (third), and PDMS encapsulation (fourth). The schematic illustration in the exploded view is shown in Fig. 4B. The fabrication processes of the deformable artificial nervous system are explained in the Supplementary Materials and fig. S11. This skin in pixelated array format can be scalably manufactured in a repeatable manner. Since all the materials are in rubbery formats, the sensory skin can be stretched (Fig. 4B). Even after 1000 times of cyclic stretching up to 50%, no mechanical damage was observed.

Figure 4C shows the schematic circuit diagram illustrating the working principle of the sensory skin from mechanoreceptors interfacing the external stimulation to synaptic nerve that resulted in excitatory postsynaptic potential (EPSP) mapping. The working mechanism and experimental result of a single channel are shown in fig. S12. Once tapping with applied pressure higher than 94 kPa on the pressure-sensitive rubber was performed, we obtained pulses with amplitudes of −3 V. The resistance change depending on applied pressure is shown in fig. S13. The pulse width is also controlled by the tapping. Once the pressure sensor is tapped, the pulse is generated to the gate electrode, and the fully rubbery synaptic transistor (biological synapse) responds with the EPSC. We obtained a 1-mV EPSP with a shunt resistor of 200 ohms based on a data acquisition system (RHD2000, Intan Technologies). The overall arrayed circuit diagram, layout, and cross-sectional view of the deformable nervous system–implemented tactile skin can be seen in figs. S14 and S15, respectively. We performed multichannel EPSP mapping after multiple-site tapping in a multiplexing manner using a data acquisition setup illustrated in fig. S16.

As a demonstration, we mapped the EPSP by tapping the sensory skin before and after applying 50% mechanical strain. As shown in Fig. 4 (D to I), by applying the tapping with objects in patterns of letters "U" (Fig. 4D) and "H" (Fig. 4E) marked within the area by red lines, we recorded the EPSP mapping. As the pressure-sensitive rubber (sensory receptor) was tapped five times successively, we obtained five successive EPSPs with a width of 50 ms. As shown in Fig. 4 (E and H), for the U and H patterns, the EPSPs ranged from 661 to 1163 μV and 756 to 1138 μV for the pixels with tapping, respectively. The EPSPs were almost 0 μV without tapping. After 50% stretch, upon tapping, the potentials ranged from 429 to 675 μV and 440 to 732 μV for U and H cases respectively, as shown in Fig. 4 (F and I, respectively). The reduced EPSPs after stretching are mainly due to the synaptic transistor other than the pressure-sensitive rubber–based mechanoreceptor. As the skin is stretched, the increases in channel resistance and, therefore, decrease in current are responsible for the EPSP decrease. However, the EPSPs remained stable after the first cycle of stretching. This stretchable neurologically integrated tactile skin could be integrated toward enabled neurologic functions in soft machines, other engineering systems, and neuroprosthetics, among others.

Soft adaptive neurorobot
We further developed a fully soft neurologically integrated robot, namely, soft neurorobot. The neurorobot is constructed on the basis of a soft pneumatic robot covered with fully rubbery elastic skin of TENGs and synaptic transistors, which are able to sense physical tapping or touches and locomote adaptively in a programmed manner through synapse memory encoded signals, as schematically illustrated in Fig. 5A. The details of the soft pneumatic robotic design, fabrication, operational principle, and photograph are presented in the Supplementary Materials and fig. S17. On the basis of the pneumatic actuations, the robot is able to perform straight walking, turning directions of left and right, etc. The fully rubbery skins sit on three sides (right, left, and top) of the robot. A detailed exploded view of the fully rubbery skins is shown in fig. S18A. The TENG generates the presynaptic pulses upon physical tapping where there is contact separation between human skin and the PDMS layer on the TENG (44). The EPSCs and short-term weight change w_n/w_1 (i.e., robotic memory) are therefore obtained from the generated presynaptic pulses. In particular, the w_n/w_1 controls the programmable robot locomotion (Fig. 5A). Figure S19 shows the photograph of TENG and synapse-enabled neurologically integrated fully rubbery robotic skin. The detailed fabrication of the soft robotic skin is presented in the Supplementary Materials. Since the TENG device has bidirectional electrical outputs as described in the following sections, rectified presynaptic pulse is critical to ensure the synaptic behaviors of the soft robotic skin. It is noted that the presynaptic pulses were rectified by a soft, full-wave diode bridge rectifier (figs. S18 and S19). The detailed circuit diagram is illustrated in fig. S18B. We used the soft Schottky diodes of P3HT-NF/Al to construct the rectifier. Figure S20 shows the schematic image and I-V characteristics of the device. Figure S21 shows the detailed TENG device structure and voltage signals before and after rectification. We chose presynaptic pulse of negative voltage for the rubbery synaptic transistor. A set of rectified presynaptic pulse and resulted EPSC are shown in fig. S22.

Figure 5B is the EPSC results after different numbers (1 to 4) of tapping. EPSCs increase as the numbers of tapping increase. The duty cycle of the presynaptic pulses from TENG is about 50% with a frequency of 5 Hz. The resulted robotic memory w_n/w_1 are 100, 140, 160, and 180% for tapping one to four times, respectively, as shown in Fig. 5C. The different w_n/w_1 controls the programmed robotic locomotion. It is noted that the skins on the left (no. 2) and right (no. 3) sides guide the robot to turn right and left correspondingly. The robot turns 10°, 20°, 30°, and 40° depending on the numbers of tapping from one to four times on the side skin. The top skin (no. 1) controls when the robot will turn on and off. When the top skin is tapped once, the robot starts to locomote. When tapped twice, the robot stops. A photograph of the soft robot turning 40° to the right after tapping the right skin four times can be seen in Fig. 5D.

The soft neurorobot is able to perform adaptive locomotion along a complex path effectively. Figure 5E shows the corresponding EPSCs of the top, left, and right skins on the soft neurorobot during its adaptive locomotion for 50 s. After the top skin was tapped once, the neurorobot started to locomote straightly. After 10 s, the left skin was then tapped once, and the neurorobot started to turn left by 10° and took 5 s to complete. The neurorobot locomoted straightly for 10 s until one tap on the right skin. The neurorobot finished turning right by 10° for around 5 s and continued to locomote straightly for another 5 s until three successive taps on the right skin were applied at the time of 35 s. The neurorobot responded correspondingly by turning right by 30° and then continued to locomote straightly for 10 s until two successive taps were applied on the top skin to allow the robot to stop. Figure 5F shows a sequence of images of the neurorobot locomotion adaptively based on the robotic memory signals.
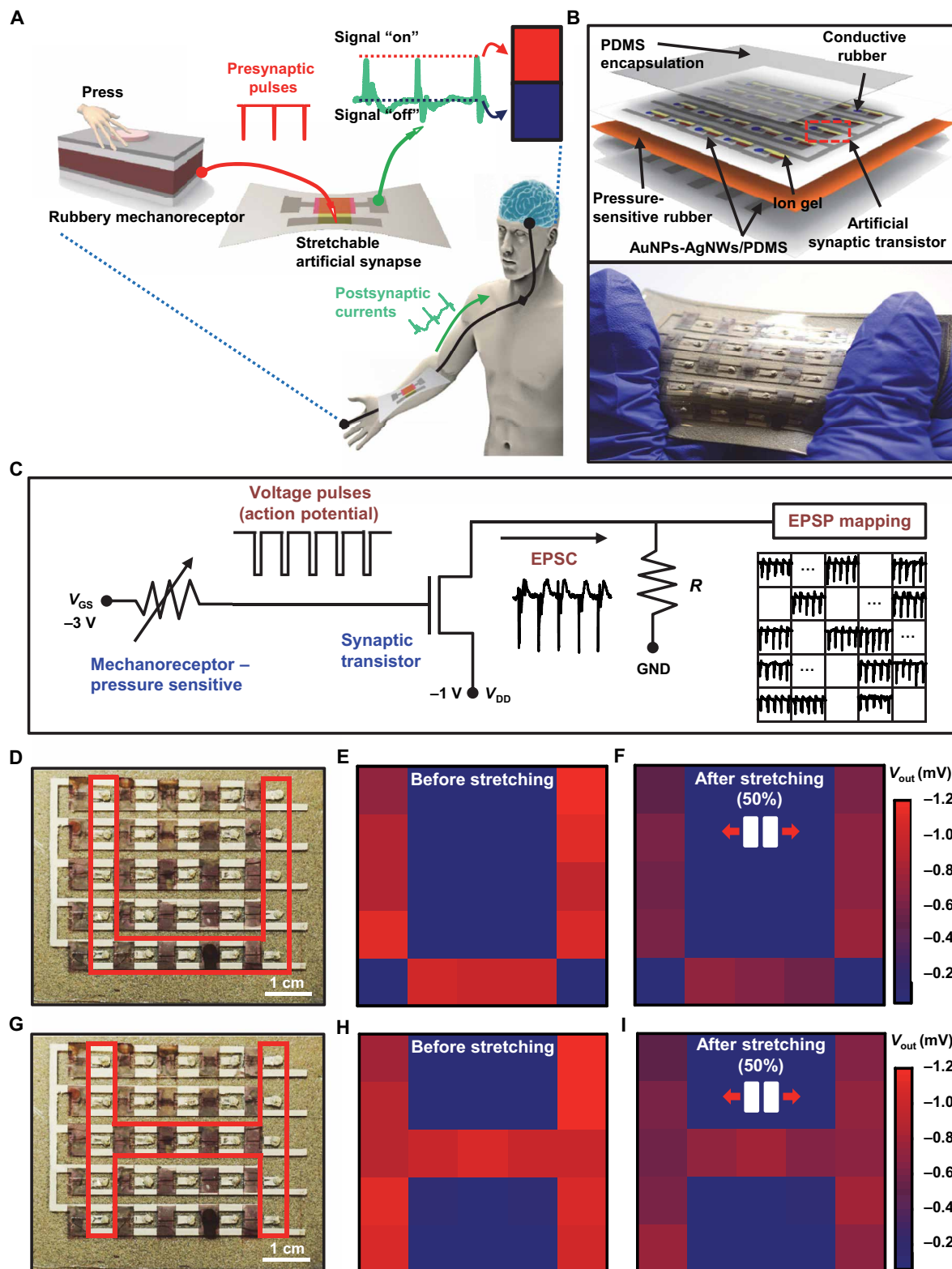
Fig. 4. Deformable neurologically integrated tactile sensory skin. (**A**) Schematic illustration of a biological somatic sensory system with mechanoreceptor and synapse-enabled skin. (**B**) Schematic exploded view (top) and optical image (bottom) of the neurologically integrated tactile sensory skin. (**C**) Schematic circuit diagram of the sensory skin from mechanoreceptors interfacing with the external stimulation to synaptic nerve that resulted in excitatory postsynaptic potential (EPSP) mapping. (**D**) Optical image of the sensory skin with applied tapping with objects in the pattern of U character. (**E** and **F**) The 5 by 5 EPSP mapping results from the stimulation in (D) for rubbery synaptic transistors before (E) and after (F) 50% strain. (**G**) Optical image of the sensory skin with applied tapping with objects in the pattern of H character. (**H** and **I**) The 5 by 5 EPSP mapping results from the stimulation in (G) for rubbery synaptic transistors before (H) and after (I) 50% strain (Photo Credit: Hyunseok Shim, University of Houston).
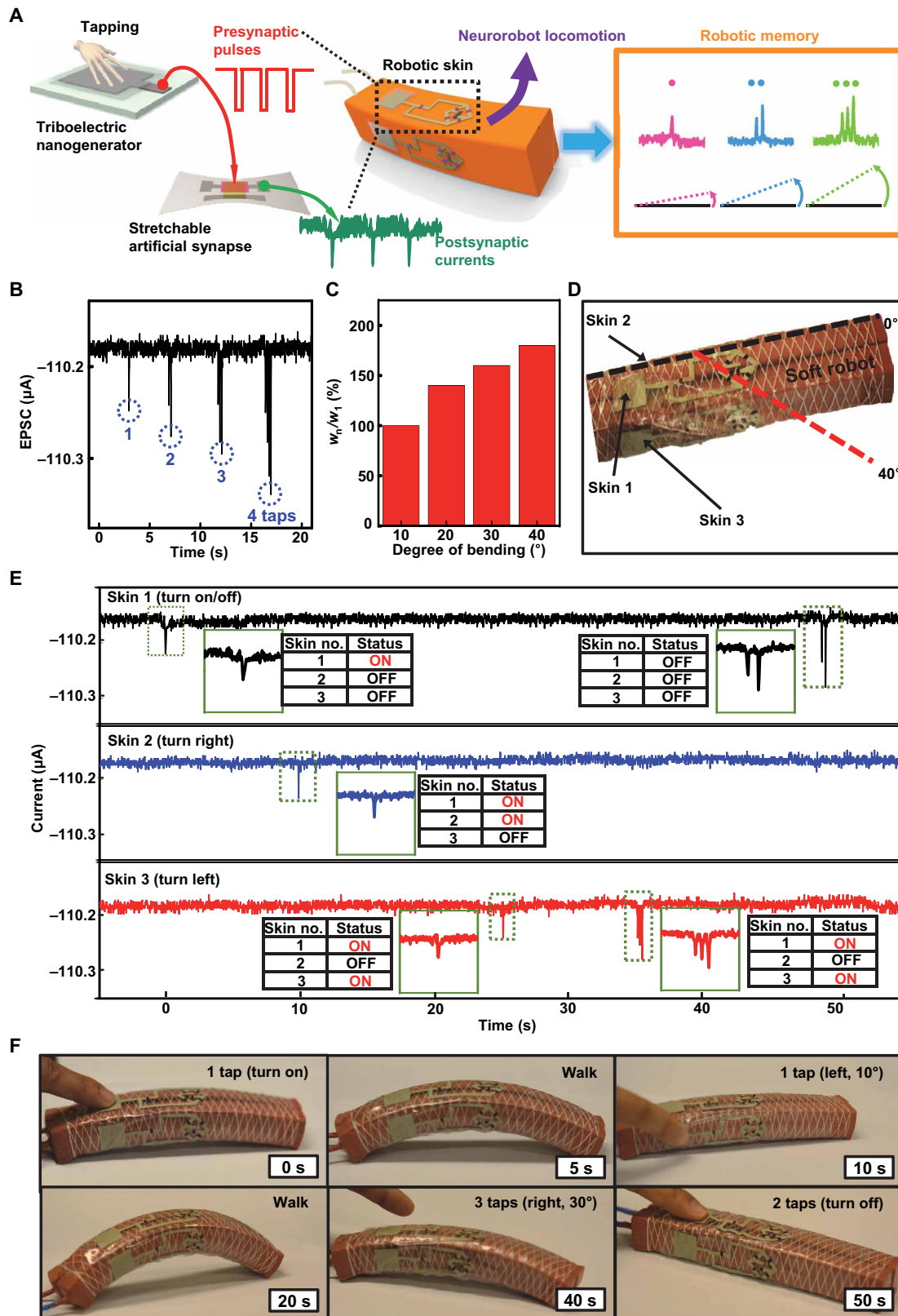
Fig. 5. Soft adaptive neurologically integrated robot. (**A**) Schematic illustration of the soft neurorobot and its programmed operation based on robotic memory decoded signals. (**B**) The EPSC after different numbers of tapping. (**C**) Programmed soft robot bending angle based on the short-term weight change (w_n/w_1). (**D**) Photograph of the soft neurorobot. (**E**) The corresponding EPSCs of the top, left, and right skins on the soft neurorobot during its adaptive locomotion for 50 s. (**F**) A sequence of images of the soft neurorobot locomotion adaptively based on the robotic memory signals in (E) (Photo Credit: Hyunseok Shim, University of Houston).

DISCUSSION

We developed a stretchable rubbery synaptic transistor inspired by soft-bodied animals. Using fully rubbery elastomeric electronic materials of the rubbery conductor, semiconductor and ion gels allow us to construct synaptic transistor with synaptic characteristics that are illustrated in a biological synapse. The characteristics of SM, STM, and LTM and filter characteristics remained even after 50% strain. Neurologically integrated devices including the fully rubbery stretchable artificial synapse–implemented tactile sensory skin– and smart skin–enabled neurologically integrated adaptive soft neurorobot, just as a few examples, illustrate the usages of the fully rubbery synapses in soft engineering systems. Our work reports a soft artificial system all made out of rubbery materials with implemented neurologic functions. Although the level of complexity of the enabled neurological functions in these demonstrated engineering systems is still far lower than that in biological counterparts, it is the first step toward future sophisticated and powerful engineering systems. Constructing an artificial synaptic transistor based on fully rubbery materials inspired by nature suggests promising directions for the development of bioinspired nervous systems with a broad range of applications beyond soft machines, ranging from neuromorphic computing (45) to neuroprosthetics (46).

MATERIALS AND METHODS

Preparation of AuNPs-AgNWs/PDMS conductor

The AgNWs were patterned on a glass substrate by drop-casting of the solution (Agnw-120, ACS Materials) through a shadow mask that is prepared by a programmable cutting machine (Silhouette Cameo). The sample was baked on a hot plate at 80°C for 10 min and annealed at 200°C for 30 min to enhance its electrical conductivity. PDMS precursor (weight ratio of prepolymer: curing agent is 10:1) was spin-coated on the patterned AgNWs at 300 rpm for 60 s, and then, the sample was cured in the oven at 95°C for 2 hours. Because of the relatively high viscosity of the PDMS precursor, AgNW pattern was partially filled with the PDMS precursor, which results in partially embedded AgNWs within the solidified PDMS. The solidified AgNWs embedded in PDMS were peeled off from the substrate to finalize the preparation of the AgNWs/PDMS electrode. To ensure ohmic contact between the work function of electrode and HOMO level of P3HT, AuNPs were formed on AgNWs by galvanic exchange process (33). The AuNP formation began with dropping HAuCl$_4$·3H$_2$O (0.5 mM) on top of AgNWs/PDMS electrode. After 2 min, to allow Ag-Au galvanic replacement reaction, the coated electrodes were rinsed by deionized (DI) water, followed by dropping H$_4$OH solution (28%) to dissolve the byproducts of AgCl layer on the AgNWs. Last, the preparation of AuNPs-AgNWs/PDMS electrode was completed by rinsing using DI water, drying with a N$_2$ gun, and dehydration at 90°C for 5 min.

Preparation of P3HT-NFs/PDMS semiconductor

The P3HT solution (2 mg/ml) was prepared by dissolving P3HT (6 mg) in dichloromethane (3 ml), followed by heating at 60°C, and then cooling at −20°C to form P3HT-NFs. The P3HT-NFs solution was blended with a PDMS solution (80 mg/ml) to obtain the P3HT-NFs/PDMS at the weight ratio of 1:4. The preparation of P3HT-NFs/PDMS thin film was finalized by spin-casting at 2000 rpm for 60 s, followed by thermal annealing at 90°C for 10 min.

Preparation of ion gel dielectric

To prepare the ion gel, poly(vinylidene fluoride-*co*-hexafluoropropylene), 1-ethyl-3-methylimidazolium bis(trifluoromethylsulfonyl) imide, and acetone were mixed with the weight ratio of 1:4:7 at 80°C for 8 hours. The ion gel was solidified by curing in the vacuum oven at 70°C for 12 hours after casting on a clean glass substrate.

Fabrication of fully rubbery synaptic transistor

The fabrication procedure of the fully rubbery synaptic transistor involved preparing the AuNPs-AgNWs/PDMS conductor (source and drain electrode), coating P3HT-NFs/PDMS semiconductor, and lastly laminating ion gel dielectric. The source and drain electrodes were prepared in the same manner as described above. The P3HT-NFs/PDMS semiconductor was patterned by spin-coating at 2000 rpm for 60 s through a Kapton shadow mask and dried for 10 min at 90°C. Last, a piece of the ion gel (~150 μm) was laminated on the P3HT-NFs/PDMS film to complete the fully rubbery synaptic transistor.

Material characterization and device measurements

The frequency-dependent capacitance of the ion gel was measured by an impedance analyzer (M204, Autolab). The electrical properties of the transistor and synaptic function were characterized by a semiconductor analyzer (4200SCS, Keithley Instruments Inc.). The presynaptic pulse was applied to the gate electrode using a function generator (DG4062, RIGOL Technologies Inc.), and the postsynaptic current was measured by applying a constant V_{ds} between the source and the drain using the power supply (1627A, BK Precision) in a relative humidity of 50%. The deformable tactile sensory skin's EPSP mapping was obtained on the basis of a data acquisition system (RHD2000, Intan Technologies). Dynamic presynaptic pulse and EPSC during robotic operation were measured using a programmable electrometer (6514, Keithley Instruments Inc.).

SUPPLEMENTARY MATERIALS

Supplementary material for this article is available at http://advances.sciencemag.org/cgi/content/full/5/10/eaax4961/DC1

Calculation of mobility and threshold voltage
Fabrication of deformable neurologically integrated tactile sensory skin
Design and fabrication of the soft pneumatic robot
Fabrication of robotic skin
Fig. S1. Optical image of fully rubbery electronic materials.
Fig. S2. Frequency-dependent capacitance per unit area.
Fig. S3. Schematic information of synaptic transistor.
Fig. S4. Transfer curve and mobilities of the rubbery synaptic transistor.
Fig. S5. EPSC results with respect to different pulse widths without (0%) and with 50% strain.
Fig. S6. EPSC results triggered by two successive synaptic pulses with respect to different Δt_{pre} without (0%) and with 50% strain.
Fig. S7. EPSCs under mechanical strain along the channel width direction.
Fig. S8. EPSCs induced by 20 successive presynaptic pulses with different frequencies without (0%) and with 50% strain.
Fig. S9. Memory characteristics from 20 successive presynaptic pulses with different widths without (0%) and with 50% strain.
Fig. S10. Memory characteristics with respect to the frequency of presynaptic pulses without (0%) and with 50% strain.
Fig. S11. Schematic illustration of the major fabrication steps for the tactile sensory skin.
Fig. S12. Neurologically integrated tactile sensory skin.
Fig. S13. Resistance change of the pressure-sensitive rubber sheet with respect to the applied pressure.
Fig. S14. Circuit diagram of the 5 by 5 arrayed synapse-implemented sensory skin.
Fig. S15. The schematic geometry and cross-sectional image of the rubbery tactile sensory skin.
Fig. S16. Measurement setup for EPSP mapping.
Fig. S17. Design, fabrication, and optical image of soft pneumatic robot.
Fig. S18. Synapse-implemented fully rubbery robotic skin.

REFERENCES AND NOTES

1. C. Laschi, B. Mazzolai, M. Cianchetti, Soft robotics: Technologies and systems pushing the boundaries of robot abilities. *Sci. Robot.* **1**, eaah3690 (2016).
2. D. Rus, M. T. Tolley, Design, fabrication and control of soft robots. *Nature* **521**, 467–475 (2015).
3. F. Hartmann, M. Drack, M. Kaltenbrunner, Meant to merge: Fabrication of stretchy electronics for robotics. *Sci. Robot.* **3**, eaat9091 (2018).
4. M.-M. Mesulam, From sensation to cognition. *Brain* **121**, 1013–1052 (1998).
5. G. S. Doetsch, Patterns in the brain: Neuronal population coding in the somatosensory system. *Physiol. Behav.* **69**, 187–201 (2000).
6. F. Calahorro, P. G. Izquierdo, The presynaptic machinery at the synapse of *C. elegans*. *Invert. Neurosci.* **18**, 4 (2018).
7. B. Hochner, An embodied view of octopus neurobiology. *Curr. Biol.* **22**, R887–R892 (2012).
8. K. Mizutani, T. Shimoi, Y. Kitamura, H. Ogawa, K. Oka, Identification of two types of synaptic activity in the earthworm nervous system during locomotion. *Neuroscience* **121**, 473–478 (2003).
9. C. D. Drewes, C. R. Fourtner, Stretch-sensitive neural units in the body wall of the earthworm, Lumbricus terrestris L. *J. Exp. Biol.* **65**, 39–50 (1976).
10. M. L. Schneider, C. A. Donnelly, S. E. Russek, B. Baek, M. R. Pufall, P. F. Hopkins, P. D. Dresselhaus, S. P. Benz, W. H. Rippard, Ultralow power artificial synapses using nanotextured magnetic Josephson junctions. *Sci. Adv.* **4**, e1701329 (2018).
11. Y. Kim, A. Chortos, W. Xu, Y. Liu, J. Y. Oh, D. Son, J. Kang, A. M. Foudeh, C. Zhu, Y. Lee, S. Niu, J. Liu, R. Pfattner, Z. Bao, T.-W. Lee, A bioinspired flexible organic artificial afferent nerve. *Science* **360**, 998–1003 (2018).
12. T. Ohno, T. Hasegawa, T. Tsuruoka, K. Terabe, J. K. Gimzewski, M. Aono, Short-term plasticity and long-term potentiation mimicked in single inorganic synapses. *Nat. Mater.* **10**, 591–595 (2011).
13. L. Q. Zhu, C. J. Wan, L. Q. Guo, Y. Shi, Q. Wan, Artificial synapse network on inorganic proton conductor for neuromorphic systems. *Nat. Commun.* **5**, 3158 (2014).
14. W. Xu, S.-Y. Min, H. Hwang, T.-W. Lee, Organic core-sheath nanowire artificial synapses with femtojoule energy consumption. *Sci. Adv.* **2**, e1501326 (2016).
15. Y. van de Burgt, E. Lubberman, E. J. Fuller, S. T. Keene, G. C. Faria, S. Agarwal, M. J. Marinella, A. A. Talin, A. Salleo, A non-volatile organic electrochemical device as a low-voltage artificial synapse for neuromorphic computing. *Nat. Mater.* **16**, 414–418 (2017).
16. K. Yang, S. Yuan, Y. Huan, J. Wang, L. Tu, J. Xu, Z. Zou, Y. Zhan, L. Zheng, F. Seoane, Tunable flexible artificial synapses: A new path toward a wearable electronic system. *Flexible Electron.* **2**, 20 (2018).
17. T.-S. Kim, Y. Lee, W. Xu, Y. H. Kim, M. Kim, S.-Y. Min, T. H. Kim, H. W. Jang, T.-W. Lee, Direct-printed nanoscale metal-oxide-wire electronics. *Nano Energy* **58**, 437–446 (2019).
18. W. Wang, G. Pedretti, V. Milo, R. Carboni, A. Calderoni, N. Ramaswamy, A. S. Spinelli, D. Ielmini, Learning of spatiotemporal patterns in a spiking neural network with resistive switching synapses. *Sci. Adv.* **4**, eaat4752 (2018).
19. C. Li, D. Belkin, Y. Li, P. Yan, M. Hu, N. Ge, H. Jiang, E. Montgomery, P. Lin, Z. Wang, W. Song, J. P. Strachan, M. Barnell, Q. Wu, R. S. Williams, J. J. Yang, Q. Xia, Efficient and self-adaptive in-situ learning in multilayer memristor neural networks. *Nat. Commun.* **9**, 2385 (2018).
20. N. Gong, T. Idé, S. Kim, I. Boybat, A. Sebastian, V. Narayanan, T. Ando, Signal and noise extraction from analog memory elements for neuromorphic computing. *Nat. Commun.* **9**, 2102 (2018).
21. D. Ielmini, H.-S. P. Wong, In-memory computing with resistive switching devices. *Nat. Electron.* **1**, 333–343 (2018).
22. M. A. Zidan, J. P. Strachan, W. D. Lu, The future of electronics based on memristive systems. *Nat. Electron.* **1**, 22–29 (2018).
23. Z. Wang, S. Joshi, S. Savel'ev, W. Song, R. Midya, Y. Li, M. Rao, P. Yan, S. Asapu, Y. Zhuo, H. Jiang, P. Lin, C. Li, J. H. Yoon, N. K. Upadhyay, J. Zhang, M. Hu, J. P. Strachan, M. Barnell, Q. Wu, H. Wu, R. S. Williams, Q. Xia, J. J. Yang, Fully memristive neural networks for pattern classification with unsupervised learning. *Nat. Electron.* **1**, 137–145 (2018).
24. I. Boybat, M. Le Gallo, S. Nandakumar, T. Moraitis, T. Parnell, T. Tuma, B. Rajendran, Y. Leblebici, A. Sebastian, E. Eleftheriou, Neuromorphic computing with multi-memristive synapses. *Nat. Commun.* **9**, 2514 (2018).
25. Y. Lee, T.-W. Lee, Organic synapses for neuromorphic electronics: From brain-inspired computing to sensorimotor nervetronics. *Acc. Chem. Res.* **52**, 964–974 (2019).
26. M. M. Shanechi, A. L. Orsborn, H. G. Moorman, S. Gowda, S. Dangi, J. M. Carmena, Rapid control and feedback rates enhance neuroprosthetic control. *Nat. Commun.* **8**, 13825 (2017).
27. T. Gulati, D. S. Ramanathan, C. C. Wong, K. Ganguly, Reactivation of emergent task-related ensembles during slow-wave sleep after neuroprosthetic learning. *Nat. Neurosci.* **17**, 1107–1113 (2014).
28. S. P. Lacour, G. Courtine, J. Guck, Materials and technologies for soft implantable neuroprostheses. *Nat. Rev. Mater.* **1**, 16063 (2016).
29. H. Wood, Achieving complex control of a neuroprosthetic arm. *Nat. Rev. Neurol.* **9**, 62 (2013).
30. M. Yang, X. Zhao, Q. Tang, N. Cui, Z. Wang, Y. Tong, Y. Liu, Stretchable and conformable synapse memristors for wearable and implantable electronics. *Nanoscale* **10**, 18135–18144 (2018).
31. Y. Lee, J. Y. Oh, W. Xu, O. Kim, T. R. Kim, J. Kang, Y. Kim, D. Son, J. B.-H. Tok, M. J. Park, Z. Bao, T.-W. Lee, Stretchable organic optoelectronic sensorimotor synapse. *Sci. Adv.* **4**, eaat7387 (2018).
32. D. S. Jeong, I. Kim, M. Ziegler, H. Kohlstedt, Towards artificial neurons and synapses: A materials point of view. *RSC Adv.* **3**, 3169–3183 (2013).
33. T. Kim, A. Canlier, C. Cho, V. Rozyyev, J.-Y. Lee, S. M. Han, Highly transparent Au-coated Ag nanowire transparent electrode with reduction in haze. *ACS Appl. Mater. Interfaces* **6**, 13527–13534 (2014).
34. F. Yu, L. Q. Zhu, W. T. Gao, Y. M. Fu, H. Xiao, J. Tao, J. M. Zhou, Chitosan-based polysaccharide-gated flexible indium tin oxide synaptic transistor with learning abilities. *ACS Appl. Mater. Interfaces* **10**, 16881–16886 (2018).
35. J. Zhu, Y. Yang, R. Jia, Z. Liang, W. Zhu, Z. U. Rehman, L. Bao, X. Zhang, Y. Cai, L. Song, R. Huang, Ion gated synaptic transistors based on 2D van der Waals crystals with tunable diffusive dynamics. *Adv. Mater.* **30**, 1800195 (2018).
36. J. Y. Oh, S. Rondeau-Gagné, Y.-C. Chiu, A. Chortos, F. Lissel, G.-J. N. Wang, B. C. Schroeder, T. Kurosawa, J. Lopez, T. Katsumata, J. Xu, C. Zhu, X. Gu, W.-G. Bae, Y. Kim, L. Jin, J. W. Chung, J. B.-H. Tok, Z. Bao, Intrinsically stretchable and healable semiconducting polymer for organic transistors. *Nature* **539**, 411–415 (2016).
37. L. F. Abbott, W. G. Regehr, Synaptic computation. *Nature* **431**, 796–803 (2004).
38. P. Feng, W. Xu, Y. Yang, X. Wan, Y. Shi, Q. Wan, J. Zhao, Z. Cui, Printed neuromorphic devices based on printed carbon nanotube thin-film transistors. *Adv. Funct. Mater.* **27**, 1604447 (2017).
39. J. Jiang, J. Guo, X. Wan, Y. Yang, H. Xie, D. Niu, J. Yang, J. He, Y. Gao, Q. Wan, 2D MoS$_2$ neuromorphic devices for brain-like computational systems. *Small* **13**, 1700933 (2017).
40. V. A. Klyachko, C. F. Stevens, Excitatory and feed-forward inhibitory hippocampal synapses work synergistically as an adaptive filter of natural spike trains. *PLOS Biol.* **4**, e207 (2006).
41. H. Watanabe, T. Takaya, T. Shimoi, H. Ogawa, Y. Kitamura, K. Oka, Influence of mRNA and protein synthesis inhibitors on the long-term memory acquisition of classically conditioned earthworms. *Neurobiol. Learn. Mem.* **83**, 151–157 (2005).
42. A. Kauffman, L. Parsons, G. Stein, A. Wills, R. Kaletsky, C. Murphy, *C. elegans* positive butanone learning, short-term, and long-term associative memory assays. *J. Vis. Exp.*, e2490 (2011).
43. E. L. Ardiel, C. H. Rankin, An elegant mind: Learning and memory in *Caenorhabditis elegans*. *Learn. Mem.* **17**, 191–201 (2010).
44. S. W. Chen, X. Cao, N. Wang, L. Ma, H. R. Zhu, M. Willander, Y. Jie, Z. L. Wang, An ultrathin flexible single-electrode triboelectric-nanogenerator for mechanical energy harvesting and instantaneous force sensing. *Adv. Energy Mater.* **7**, 1601255 (2017).
45. Y. van de Burgt, A. Melianas, S. T. Keene, G. Malliaras, A. Salleo, Organic electronics for neuromorphic computing. *Nat. Electron.* **1**, 386–397 (2018).
46. Y. Wu, Y. Liu, Y. Zhou, Q. Man, C. Hu, W. Asghar, F. Li, Z. Yu, J. Shang, G. Liu, M. Liao, R.-W. Li, A skin-inspired tactile sensor for smart prosthetics. *Sci. Robot.* **3**, eaat0429 (2018).
47. T. Wang, L. Ge, G. Gu, Programmable design of soft pneu-net actuators with oblique chambers can generate coupled bending and twisting motions. *Sens. Actuators A Phys.* **271**, 131–138 (2018).
48. L. Ge, T. Wang, N. Zhang, G. Gu, Fabrication of soft pneumatic network actuators with oblique chambers. *J. Vis. Exp.*, e58277 (2018).
49. P. Polygerinos, Z. Wang, J. T. B. Overvelde, K. C. Galloway, R. J. Wood, K. Bertoldi, C. J. Walsh, Modeling of soft fiber-reinforced bending actuators. *IEEE Trans. Robot.* **31**, 778–789 (2015).

Citation: H. Shim, K. Sim, F. Ershad, P. Yang, A. Thukral, Z. Rao, H.-J. Kim, Y. Liu, X. Wang, G. Gu, L. Gao, X. Wang, Y. Chai, C. Yu, Stretchable elastic synaptic transistors for neurologically integrated soft engineering systems. *Sci. Adv.* **5**, eaax4961 (2019).

Science Advances

Stretchable elastic synaptic transistors for neurologically integrated soft engineering systems

Hyunseok Shim, Kyoseung Sim, Faheem Ershad, Pinyi Yang, Anish Thukral, Zhoulyu Rao, Hae-Jin Kim, Yanghui Liu, Xu Wang, Guoying Gu, Li Gao, Xinran Wang, Yang Chai and Cunjiang Yu

ARTICLE TOOLS	http://advances.sciencemag.org/content/5/10/eaax4961
SUPPLEMENTARY MATERIALS	http://advances.sciencemag.org/content/suppl/2019/10/07/5.10.eaax4961.DC1
REFERENCES	This article cites 47 articles, 7 of which you can access for free http://advances.sciencemag.org/content/5/10/eaax4961#BIBL
PERMISSIONS	http://www.sciencemag.org/help/reprints-and-permissions

Use of this article is subject to the Terms of Service